Journal of Geophysical Research: Earth Surface

RESEARCH ARTICLE
10.1029/2018JF004636

Key Points:
- Suspended sediment loads and onshore transport rates were larger for plunging than for spilling breakers
- Turbulent kinetic energy arrived earlier on the wave phase for plunging compared to spilling breakers
- Instantaneous suspended sediment loads were linearly related to instantaneous turbulent kinetic energy

Correspondence to:
T. Aagaard,
taa@ign.ku.dk

Citation:
Aagaard, T., Hughes, M. G., & Ruessink, G. (2018). Field observations of turbulence, sand suspension, and cross-shore transport under spilling and plunging breakers. *Journal of Geophysical Research: Earth Surface*, *123*, 2844–2862. https://doi.org/10.1029/2018JF004636

Received 1 FEB 2018
Accepted 11 OCT 2018
Accepted article online 25 OCT 2018
Published online 9 NOV 2018

©2018. American Geophysical Union. All Rights Reserved.

Field Observations of Turbulence, Sand Suspension, and Cross-Shore Transport Under Spilling and Plunging Breakers

Troels Aagaard[1], Michael G. Hughes[2,3], and Gerben Ruessink[4]

[1]Institute of Geoscience and Natural Resources, University of Copenhagen, Copenhagen, Denmark, [2]Science Division, NSW Office of Environment and Heritage, Sydney, New South Wales, Australia, [3]School of Earth and Environmental Sciences, University of Wollongong, North Wollongong, New South Wales, Australia, [4]Department of Physical Geography, Faculty of Geosciences, Utrecht University, Utrecht, Netherlands

Abstract Measurements of wave orbital velocity, near-bed turbulence levels, and sediment suspension were obtained under plunging and spilling breakers in the outer surf zone on the beach at Vejers, Denmark. For the same range of relative wave heights and indicators of wave nonlinearity, we observed significantly larger suspended sediment concentrations and onshore-directed rates of suspended sediment transport under (long period) plunging breakers, compared to (short period) spilling breakers. This is consistent with the long-held understanding that, for a given beach slope, onshore transport and beach accretion are associated with longer-period waves and offshore transport and erosion are associated with shorter-period waves. An intra-wave analysis of hydrodynamics and sediment suspension revealed that the main reason for the larger suspended sediment transport rates under plunging waves was (i) larger time-averaged suspended sediment loads under plunging waves, and (ii) a larger difference in cumulated sediment load under the wave crest phase compared to the wave trough phase for plunging breakers. This latter difference was due to an earlier arrival at the seabed of higher levels of turbulent kinetic energy under plunging waves compared to spilling waves. Hence, both magnitude and timing within the wave cycle of turbulent kinetic energy production are important in a quantification of sediment transport under breaking waves. For ensemble-averaged intense suspension events, contributing roughly 50% of the total sediment suspension during individual records, we found that instantaneous near-bed sediment load was linearly related to instantaneous levels of Froude-scaled turbulent kinetic energy.

1. Introduction

Beaches tend to erode during high-energy storm conditions and recover during intervening fair-weather and moderate wave energy conditions. The net transport of sand causing this behavior depends mainly on the balance between transport due to mean flows and oscillatory transport due to incident wind and swell waves. During erosion events, the former dominates and seaward transport of sand is associated with strong, offshore-directed currents such as undertow. On the other hand, the recovery process, which is essential for the existence of subaerial beaches, is typically driven by onshore sand transport associated with incoming short waves, and this transport must be of a magnitude sufficient to overcome offshore transport driven by undertow. While this has been known for a long time, our understanding and predictive capability as to how, why, and when this net onshore feed of sand takes place through a surf zone is still limited. Presently available sediment transport and morphodynamic models experience problems with simulating onshore sand transport driven by oscillatory flows under natural field conditions (e.g., Austin et al., 2009; Henderson et al., 2004; Marino-Tapia et al., 2007; Ruessink et al., 2007). An important reason for this is that a simple in-phase relationship between instantaneous (oscillatory) cross-shore velocity and instantaneous suspended sediment load rarely exists, such as assumed by, for example, time-dependent energetics models (e.g., Bailard, 1981; Marino-Tapia et al., 2007). Surf zone processes such as wave breaking and wave-current interaction, as well as nearshore bedforms, all introduce complexities to this phase relationship (e.g., Aagaard & Hughes, 2010; Brinkkemper et al., 2017; van der Werf et al., 2007), and further complications arise because of the relatively fine grain sizes in many natural surf zones that introduce time lags associated with suspended sediment settling.

These complications render prediction of (onshore-directed) wave-driven sediment transport during beach recovery difficult. In the aftermath of storm events, surf zone wave and roller heights decrease, which lead to reduced undertow speed such that oscillatory wave motions may become the dominant transport mechanism. Furthermore, decreasing wave steepness associated with longer (swell) periods often causes wave breaking to become mainly of the plunging rather than the spilling type that tends to dominate during erosive storm conditions. The dominance of oscillatory motions implies that intra-wave and intra-wave group timescales and processes become important, the resolution of which requires an investigative approach that is wave phase resolving rather than time averaging. In order to understand and predict oscillatory (intra-wave) sand transport under conditions of beach accretion, it is therefore necessary to understand and model satisfactorily the phase relationships between the oscillatory flow and the suspended sediment load under different breaking wave conditions.

Intra-wave suspended sediment load depends on sediment settling velocity, which again depends on grain size, and sediment diffusivity, which represents a variety of vertical mixing mechanisms. In the surf zone, vertical mixing is caused by both turbulence injection from breaking waves and from fluid interaction with the seabed (e.g., Grasso & Ruessink, 2012). Recent field (Aagaard & Hughes, 2010; Ruessink, 2010; Scott et al., 2009) and laboratory (Brinkkemper et al., 2016; Shin & Cox, 2006; van der A et al., 2017) work has shown that surface-injected breaker turbulence may impinge on the seabed and stir the sediment. There are also indications that near-bed sediment diffusivity may be significantly underestimated in many models, particularly when the breaking waves are of the plunging type (Aagaard & Jensen, 2013). Moreover, not only the magnitude but also the timing of turbulence injection into the water column are critical to an understanding and parameterization of intra-wave sediment transport (Brinkkemper et al., 2017; Scott et al., 2009).

Recently, several large-scale laboratory experiments using regular (van der A et al., 2017; van der Zanden et al., 2016, 2018) and irregular (Brinkkemper et al., 2016) waves have revealed details on the turbulent velocity field, in particular under plunging breakers. Plunging breakers may generate large-scale coherent vortices, which exhibit a rotational velocity field with brief but intense downward motion from the plunging jet on the front face of the wave, followed by upward motion from the ascending vortex limb (Aagaard & Hughes, 2010; Ting, 2013). At the wave breakpoint, turbulent kinetic energy (TKE) increases steadily from the wave trough and reaches a peak at the zero-velocity upcrossing on the wave front (van der Zanden et al., 2018). Laboratory experiments by LeClaire and Ting (2017) have shown that the vortex timescale under plunging waves is large, typically in the order of $T/2$ where T is the wave period, while the vortex diameter is in the order of 0.5 h, where h is the water depth. Vortex sweeps from the plunging jet initiate sediment suspension, and sand may be subsequently lifted by the ensuing ejection and bed suction (Sumer et al., 2013). Since turbulence injection and hence sediment suspension tend to occur mainly on the front of the wave and preceding the wave crest phase, this could cause large onshore transport of suspended sediment.

Less recent attention has been paid to turbulence under spilling breakers and surf zone bores. Nadaoka et al. (1989) observed obliquely descending vortices behind the crest of spilling waves, and spilling breakers exhibit turbulent length scales that are significantly smaller than in plunging waves, 0.1–0.2 h (Ting & Kirby, 1996). Hence, it might be expected that downward propagation of these vortices would result in a time lag between orbital velocity and arrival of surface-generated turbulence at the bed. Laboratory measurements inside the surf zone by Cox and Kobayashi (2000; their Figures 3 and 4) showed that turbulence typically arrived after the passage of the wave crest. Hence, mobilization of suspended sediment would be expected to occur later in the wave phase than for plunging breakers, potentially causing significantly reduced onshore wave-driven sediment transport rates compared to plunging wave cases.

Most of the works cited above used regular laboratory waves and typically fixed beds. The main aim of this study is to use field measurements to examine the relationships between breaker type, turbulence magnitude and timing, and cross-shore suspended sediment transport on a natural beach subjected to irregular waves. The measurements of hydrodynamics and sediment suspension within the lower ≈ 25 cm of the water column under breaking waves showed that systematically larger onshore-directed oscillatory suspended sediment transport rates occurred under plunging breakers compared to spilling breakers. We will then explore the hypothesis that this can be explained in terms of both different near-bed turbulence intensities and timing within the wave cycle of turbulence injection and ensuing sediment suspension

Figure 1. Plunging breaker at the shorebreak at Vejers. Landward of the shorebreak, a surf bore is propagating onshore in the inner surf zone. In the background, an outer breaker zone is located over the inner subtidal bar.

under plunging breakers generated by long-period swell, and under spilling breakers generated by shorter-period wind waves.

2. Field Site and Instrumentation

The field campaign took place in September–October 2007 at the modally intermediate-state beach of Vejers on the exposed North Sea coast of Denmark. The beach is exposed to the west with a shore-normal oriented 285°N. The shore-normal fetch is about 600 km but almost unlimited in a northwesterly direction. The mean annual offshore significant wave height measured by a Waverider buoy 8.5 km from the beach in 16-m water depth is $H_{s,0}$ = 1.3 m and the maximum annual $H_{s,0} > 7$ m. The nearshore wave field consists of mainly locally generated wind waves but with a significant swell component ($H_{s,0}$ ~ 0.5–1 m) that becomes dominant during periods with weak or offshore winds. The semidiurnal tides exhibit spring and neap ranges of approximately 1.2 and 0.6 m, respectively. The upper shoreface contains a multiple-bar system comprising three to four nearshore bars, and the waves typically break by plunging on bars while they reform in deep and wide troughs between the bars and finally break through plunging or spilling near the boundary between the subtidal and intertidal zones, which is here termed the shorebreak (Figure 1). After the shorebreak, waves propagate onshore as surf bores prior to transforming into swash. During the field campaign, the mean sediment grain size in the breaker/surf zones was $\overline{D}$ = 0.22 mm, corresponding to a mean settling velocity w_s = 0.025 m/s.

A cross-shore array of four instrument stations was installed in the intertidal and subtidal zones, see Figure 2. The stations consisted of stainless steel H-frames, and each station held a pressure sensor (Druck Model PTX1830) and a 3-D sideways-looking Sontek 10 MHz Acoustic Doppler Velocimeter (ADVField), which was deployed close to the bed at a nominal elevation of z = 0.03–0.05 m. The velocity sensors were installed to measure positive flows onshore, to the north, and upward. Data used in this paper were collected at the main instrument station, which was located on a steeply sloping segment (β = 0.06) of the profile near the shorebreak position. Along with the pressure and ADV sensors, this station held a vertical array of six optical backscatter (OBS-1P) sensors for measuring sediment concentration. These sensors were spaced at 5 cm in the vertical, with the lowermost sensor at a nominal elevation of z = 0.05 m. When the stations could be accessed, instrument elevations were measured and, if necessary, adjusted prior to instrument runs. All instruments were hard wired to shore-based data acquisition systems and sampled at 16 Hz, and data records had a

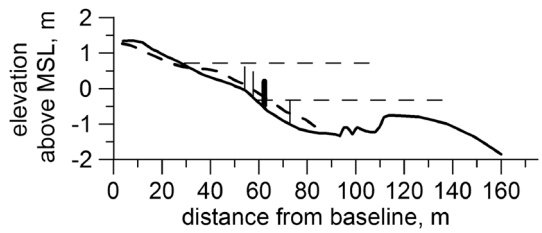

Figure 2. The cross-shore profile at the measurement site at the beginning (22 September; dashed line) and end (2 October; solid line) of the field campaign. The vertical bars indicate positions of instrument stations with the main station highlighted. The horizontal dashed lines indicate mean high and low tide levels. MSL = mean sea level.

duration of 45 min. A cross-shore profile at the instrument transect was surveyed at every daily low tide using Real Time Kinematic GPS (RTK-GPS).

During the 2-week long field campaign at Vejers, wave conditions were moderate. $H_{s,0}$ = 1–2 m and zero-crossing wave periods were typically T_z = 5–6 s for the records used in this paper (Figure 3). Wave incidence angles were mostly between west and north. The wave field consisted of a mixture of locally generated wind waves and swell; quasi-regular long-period swell was dominant inshore during weak or offshore winds. Waves were strongly attenuated by breaking across the nearshore bar system, and the maximum significant wave height recorded at the instrument station was therefore no more than H_s = 0.7 m. Over a tidal cycle, and depending on the incoming wave height, shoaling waves, breaking waves (plunging or spilling at the shorebreak; Figure 1), surf bores, and swash were all observed at the main instrument station. During the course of the experiment, net onshore transport at the instrument array caused onshore migration of the intertidal bar located between mean high and low tide levels (Figure 2) and transformation of the bar into a berm (Jensen et al., 2009).

3. Methods

3.1. Data Processing

In highly turbulent and/or aerated surf zone flows, velocity records from acoustic velocity sensors often become noisy. Potentially flawed velocity data points were corrected by signal despiking and subsequent data filtering. In the case of cross-shore (u) and alongshore (v) flows, record spikes were identified as cases when the change in velocity between two data points ($u_i - u_{i-1}$) exceeded $2.5\sigma_{(u)}$, where σ is the velocity standard deviation. Spikes were replaced by a linearly interpolated velocity. In the surf zone, vertical velocity (w) components are more spiky than horizontal components because the small (oscillatory) background signal is perturbed by sudden turbulent bursts, and the threshold used to identify signal spikes was in this case $(w_i - w_{i-1}) > g$. Careful inspection confirmed that these procedures satisfactorily removed unwanted noise spikes. Subsequently, along-beam correlation between successive acoustic returns was used to identify potentially incorrect data points with a signal correlation threshold given by $0.3 + 0.4\sqrt{\frac{sf}{25}}$ (Elgar et al., 2005), where sf is the sampling frequency. A low-pass filtered record of the despiked velocity time series was constructed by using a four-point moving average filter, and when signal correlation was below the threshold, data points in the despiked velocity time series were replaced by the corresponding observation from the low-pass filtered time series (Aagaard & Hughes, 2010). The vertical velocity component required further processing since these estimates are strongly sensitive to small vertical alignment errors. Even small tilts of the sensor will cause significant bias because large horizontal velocities are aliased into the smaller vertical velocity component. Since perfect alignment is near-impossible in the field, and since sensors were installed over a sloping bed, which will potentially cause the main flow axis to deviate from the horizontal, tilt bias invariably existed in the records. To remove such bias, velocity data were rotated onto the principal bed-parallel and bed-normal axes following the procedure outlined in Emery and Thompson (2001).

The optical backscatter sensors were calibrated after the experiment in a large recirculation tank (over the range $\overline{C}$ = 0–60 kg/m^3) using sand samples from the field deployment location. All sensors calibrated linearly with an $r^2 > 0.99$. For each field data record, field offsets, which may be caused by instrument electronics and/or quasi-steady background turbidity from organics or washload, were determined from the inflection point in the cumulative frequency distributions of sediment concentrations and subtracted from the records (Aagaard & Jensen, 2013). Field offsets were in the range of 2–5% of the cumulative frequency distribution.

After calibration, the OBS records were visually screened and checked for data quality. Field records that contained obvious noise and/or erroneous data were rejected. Further selection criteria included the following (Aagaard & Jensen, 2013): (i) OBS records that displayed nonsteady offsets, which may be indicative of temporary sensor-bed interference, were rejected; (ii) manual measurements of instrument elevation above the bed were required for each low tide during a data collection sequence, such that instrument elevation could

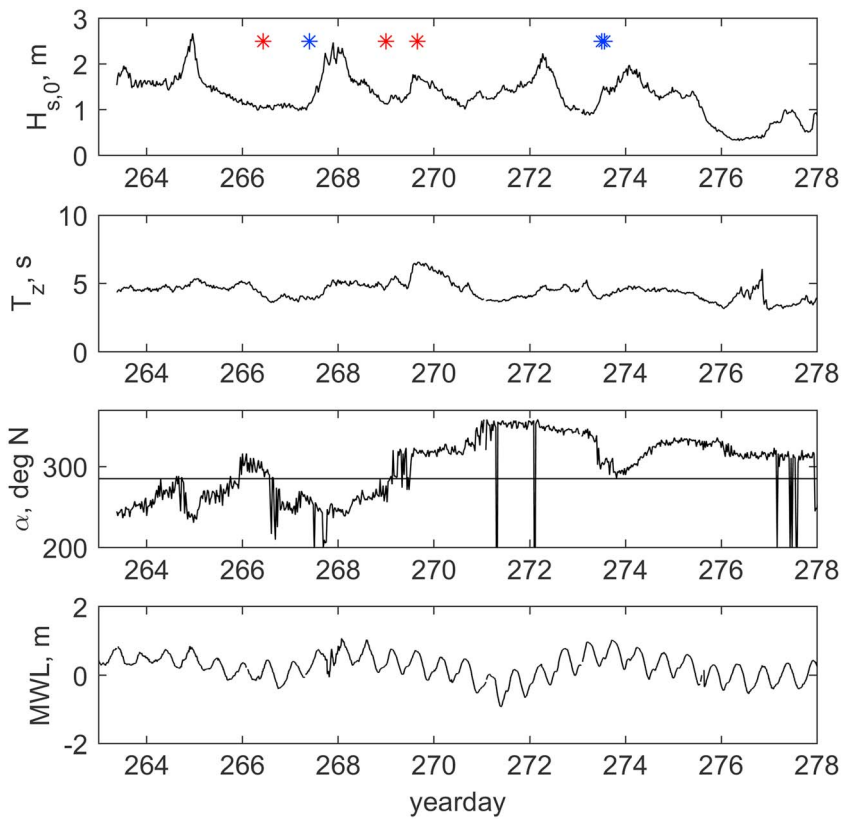

Figure 3. Offshore significant wave height ($H_{s,0}$), zero-crossing wave period (T_z), and wave incidence angle (α), all at h = 16 m during the field campaign. In the latter, the horizontal line shows the orientation of the shore normal. The lower panel shows mean water level (MWL) measured at Hvide Sande Harbour, 45 km north of the field site. The asterisks mark the timing of the instrument records used in this paper. Red indicates plunging breaker cases, and blue is used for spilling breaker cases. Note that two of the spilling cases are very close since they were recorded 2 hr apart.

be estimated at all times (see below); and (iii) at least four out of the six sediment concentration time series in the vertical sensor array should be devoid of bubble signatures. When OBS1-P sensors are covered by less than 0.05–0.1 m of water, they may be significantly affected by foam, which is propagating onshore on the crest of surf bores. Such cases are relatively easy to identify visually as instrument time series become very spiky and repeatedly attain saturation levels, typically under each wave crest. Air bubble- or foam-affected time series were identified and subsequently rejected if (iv) mean sediment concentration for a given sensor was larger than the mean concentration recorded at a lower sensor, and (v) a cross-correlation analysis between one sensor and another mounted nearer the seabed exhibited a negative phase lag. Finally, (vi) vertical mean sediment concentration profiles for a given record, which were typically exponential, or Rouse shaped, should exhibit an $r^2 > 0.9$ for the best least squares fit equation.

3.2. Data Selection

From the corrected and reduced data set, a limited number of records were selected for analysis. The selection criteria were as follows: (i) the main instrument station was located near the mean shorebreak position, and breaking waves occurred rather than surf bores, that is, the station was located in the outer surf zone; (ii) a firm visual identification of the dominant type of breaking (plunging or spilling); and (iii) near-similar ADV and OBS elevations in all selected records, with the ADV and the lowermost OBS sensor as close as possible to the bed without interfering with the flow, z = 0.035–0.07 m. Since it was difficult, or impossible, to confidently measure instrument elevations except at low tide, elevations at mid and high tides were calculated from the sediment continuity approach described in Aagaard and Jensen (2013).

Few records met all criteria, not least because of the tidally induced cross-shore translation of the shorebreak, and since an equal number of spilling and plunging cases was desirable, only six records were deemed

Table 1
Inshore Waves and Currents at the Main Instrument Station for the Selected Instrument Runs

	H_s (m)	T_p (s)	h (m)	H_s/h	u_s (m/s)	U (m/s)	V (m/s)	ψ	ξ	SK_u	AS_u	$\lvert\overline{\tau}\rvert$	$\overline{k}$	Ω
Plunging cases														
PL3	0.41	11.6	0.65	0.63	0.79	−0.05	+0.09	175	0.43	0.27	0.69	2.24	0.024	1.41
PL28	0.45	17.4	0.50	0.90	0.95	−0.27	−0.16	253	0.45	0.31	0.68	5.51	0.043	1.03
PL36	0.65	14.8	1.06	0.61	0.94	−0.18	−0.40	248	0.41	0.11	−0.23	3.88	0.023	1.76
Spilling cases														
SP16	0.40	7.0	0.55	0.72	0.93	−0.02	+0.26	243	0.31	0.28	0.68	2.2	0.024	2.29
SP42	0.41	6.9	0.63	0.66	0.82	−0.07	−0.11	189	0.28	0.31	0.55	1.63	0.020	2.38
SP44	0.47	5.1	0.82	0.58	0.84	−0.08	−0.11	198	0.24	0.30	0.37	1.53	0.017	3.69

Note. Significant wave height (H_s), peak spectral wave period (T_p), mean water depth (h), relative wave height (H_s/h), maximum orbital velocity ($u_s = 2\sigma_u$), mean cross-shore (U) and longshore (V) current speed, wave mobility number ($\psi = u_s^2/(s-1)gD$, where $(s-1)$ is the relative sediment density and D is the mean grain size), Iribarren number (ξ), cross-shore velocity (SK_u) and acceleration (AS_u) skewness, mean (absolute) Reynolds stress ($\lvert\overline{\tau}\rvert$), Froude-scaled TKE ($\overline{k}$), and the Gourlay parameter $\Omega = H_s/w_sT$, where w_s is sediment settling velocity. TKE = turbulent kinetic energy.

suitable for analysis: Three records representing plunging breakers (PL cases), and three representing spilling breakers (SP cases). The timings of these selected records are indicated in Figure 3, and Table 1 lists the hydrodynamic conditions at the main instrument station. Local significant wave height ($H_s = 4\sigma_\eta$, where σ_η is the standard deviation of water surface elevation) ranged between H_s = 0.4 and 0.65 m and water depths h = 0.5–1.06 m. Maximum orbital velocity magnitude and hence wave mobility numbers occupied the same ranges for the PL and SP cases. The mobility numbers indicate that bedforms were typically transitional between (anorbital) wave ripples and flat beds (Dingler & Inman, 1976; Hay & Mudge, 2005), which is consistent with occasional field observations. Incoming wave orbital velocity skewness (SK_u) was calculated as

$$SK_u = \frac{< u^3 >}{(< u^2 >)^{1.5}} \tag{1}$$

where cross-shore velocity (u) was determined for frequencies $f > 0.05$ Hz using high-pass filtered velocity records (to avoid effects from infragravity waves and mean currents), and the brackets denote the time average. Acceleration skewness (velocity asymmetry; AS_u) was calculated similarly with u (in equation (1)) replaced by its temporal derivative. These quantities also did not differ significantly for PL and SP cases (Table 1). Only the spectral wave peak periods were systematically different for the two groups of data; T_p = 5–7 s for the SP cases (wind waves) and T_p = 11–17 s for the PL cases (swell).

It has earlier been shown (Battjes, 1974) that in idealized laboratory settings, the local Iribarren number is successful in distinguishing between spilling and plunging breakers. To confirm the visual observations of breaker type, this was calculated as

$$\xi = \frac{\tan\beta}{\sqrt{H_s/L_0}} \tag{2}$$

where β is the local cross-shore bed slope, determined over a 10-m distance centered on the instrument station, and L_0 is the deep-water wavelength ($L_0 = (g/2\pi)T_z^2$, where T_z is the zero-crossing wave period). H_s was determined from high-pass filtered pressure records to avoid infragravity wave effects in the quantification of breaking wave type. The zero-crossing wave period was determined from $T_z = (m_0/m_2)^{1/2}$ where m_0 and m_2 are the zeroth and second moments of the wave spectrum. For PL cases $\xi > 0.4$, while $\xi < 0.35$ for the SP cases (Table 1), which is consistent with the limiting value of $\xi = 0.4$ found by Battjes (1974).

3.3. Analysis Techniques

To examine the relationships between turbulence and sediment suspension and transport, the turbulent component of the velocity field needs to be extracted and isolated from the oscillatory motions, which is not straightforward. Ensemble averaging of the velocity signal is often applied as a separation technique for regular waves in the laboratory, but this is difficult with irregular waves in the field. The velocity-

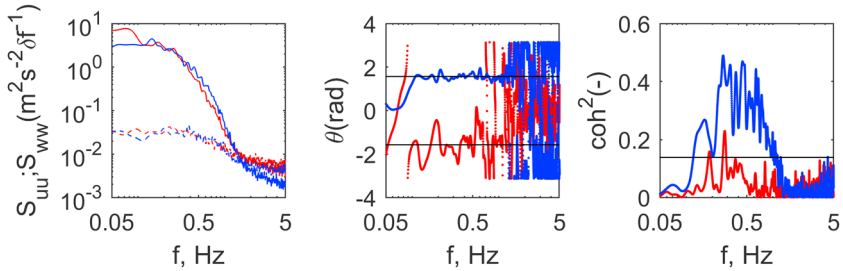

Figure 4. (left panel) Spectra of cross-shore (S_{uu}; solid lines) and vertical (S_{ww}; dashed lines) velocities for a plunging breaker case (PL36; red lines) and a spilling breaker case (SP16; blue lines), (middle panel) cross-spectral *u/w* phases and (right panel) squared coherence. The spectra were computed with 200 degrees of freedom. The horizontal lines indicate phases of $\pm\pi/2$ in the phase plot and the 95% confidence level in the coherence plot.

differencing technique (Brinkkemper et al., 2016; Shaw & Trowbridge, 2001) requires two, or more, velocity sensors that are separated in the vertical, or horizontal, at the same cross-shore position. Frequency filtering techniques based on spectral slope breaks have earlier been used to define a cutoff frequency between wave orbital and turbulent motion (e.g., Foster et al., 2006; Mocke, 2001). Figure 4 shows spectral plots of the cross-shore (*u*) and vertical velocity (*w*) components for two representative SP and PL cases. The cross-shore velocity component exhibits a spectral roll-off near f^{-3}, suggesting the dominance of orbital motions over the frequency range $f \sim 0.5$–1.4 Hz where there is a break in the spectral slope. It is difficult to identify such breaks for the *w* components that are nearer a roll-off of $f^{-5/3}$ over the entire frequency range above 0.5 Hz, suggesting that turbulence dominated the vertical velocities. From these plots, it would be difficult to select a cutoff frequency. A technique that may be applied to provide guidance in the separation of (dominant) turbulent and oscillatory velocities is to examine the phase relationships between horizontal and vertical velocity components using cross-spectral analysis. Outside the wave boundary layer, organized progressive wave motion is expected to exhibit a $\pm\ \pi/2$ phase between cross-shore and vertical velocities. For the SP case, the *u/w* phase is consistently near $\pi/2$ for frequencies $f < 1.3$ Hz, while phases become erratic for higher frequencies and exhibit continuous phase wraps (Figure 4). This is indicative of turbulence dominating the velocity field at $f > 1.3$ Hz, which is consistent with the frequency at which squared coherence drops from statistically significant levels toward zero. For the PL case shown here (as well as for the other plunging wave cases), phases were less stable and coherence was lower; in Figure 4, the phase is seen to fluctuate near $-\pi/2$ up to a frequency of $f = 0.7$ Hz; beyond $f = 0.7$ Hz, the phase drifts toward $-\pi$ and phase wraps set in. Consequently, for this case, $f = 0.7$ Hz is considered to be the frequency at which turbulence begins to dominate the cospectrum.

Following extraction of the turbulent velocity components through high-pass filtering with the filter cutoff frequency (f_c) determined from the cross-spectral analysis, TKE was calculated as

$$TKE = 0.5\left(u'^2 + v'^2 + w'^2\right) \tag{3}$$

where u',v',w' are the (turbulent) cross-shore, longshore, and vertical velocities, and (record-averaged) Froude-scaled TKE was calculated as $\overline{k} = \sqrt{\overline{TKE}/(gh)}$, where an overbar indicates the time average, g is the acceleration of gravity, and h is water depth. Turbulent Reynolds shear stress was calculated as

$$|\tau| = \rho\left|u'w'\right| \tag{4}$$

where u in this case indicates the resultant vector sum (u_r) of cross-shore and longshore turbulent velocities ($u_r' = \sqrt{u'^2 + v'^2}$). Note that following Cox and Kobayashi (2000) and Chassagneux and Hurther (2014), we use the absolute value of the Reynolds shear stress since this is often related to near-bed suspended sediment concentration or to the pickup of sediment from the bed (Glenn & Grant, 1987; Nielsen, 1992). The sign is omitted since sediment grains may be mobilized on both onshore and offshore phases of the flow, and it is unclear whether mobilization occurs when vertical velocity is downward or upward directed. LeClaire and Ting (2017) observed predominant suspension events during turbulent downbursts, while the

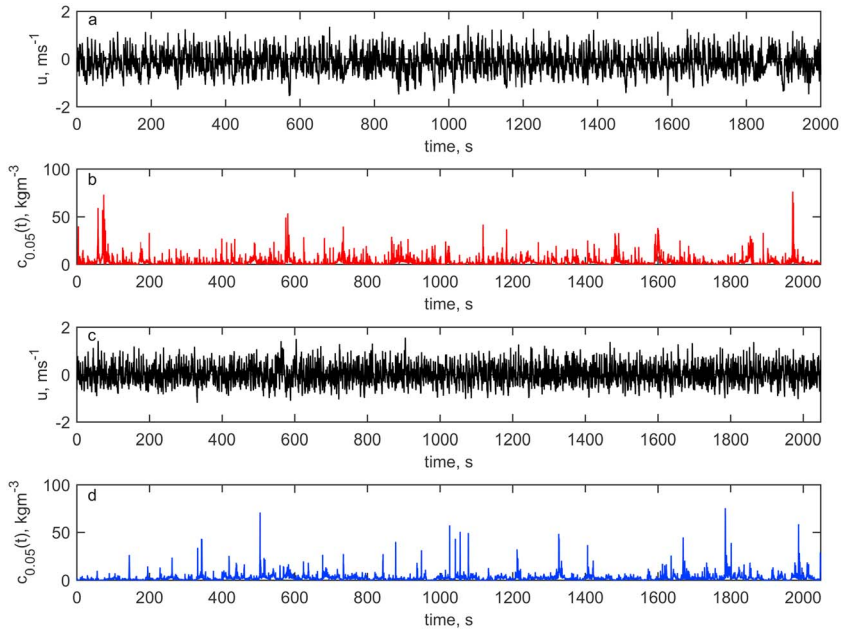

Figure 5. Time series of cross-shore velocity (u) and sediment concentration ($c_{0.05}[t]$) for cases PL36 (a, b) and SP16 (c, d).

opposite was found by Sumer et al. (2013). For our data set, $|\overline{\tau}|$ was a factor of 2 larger, on average, for PL cases compared to SP cases (Table 1), which is consistent with the larger spectral densities at high frequencies in Figure 4.

Clearly, the magnitude of both $\overline{TKE}$ and $|\overline{\tau}|$ depends significantly on the cutoff frequency (f_c) and, in particular, for the PL cases where f_c = 0.6–1.15 Hz while f_c = 1.3–1.65 Hz for the three SP cases. A 0.1-Hz increase/decrease of f_c results in approximately 40% difference in $|\overline{\tau}|$ for the PL case above, while for the SP case, the difference is about 15%. Using the same f_c for the two cases (f_c = 1.3 Hz) would still yield $|\overline{\tau}|$ roughly a factor 2.5 larger for the PL case compared to the SP case. However, given the larger turbulent length scales associated with plunging compared to spilling breakers (0.5 h versus 0.1–0.2 h; LeClaire & Ting, 2017; Ting & Kirby, 1996), f_c would indeed be expected to be significantly lower for PL than for SP cases.

4. Results

4.1. Sediment Concentration and Transport Under Spilling and Plunging Breakers

Except for the wave period, the six selected data records did not differ substantially with respect to wave conditions; the ranges of wave height (H_s), orbital velocity (u_s,) asymmetry measures (SK; AS), and mean current speeds $(\overline{U}, \overline{V})$ were largely identical for the two groups of data (Table 1). Nevertheless, mean near-bed sediment concentrations tended to be larger for the plunging cases than for the spilling cases. Time series of cross-shore velocity and sediment concentration (at z = 0.05 m) for PL36 and SP16 are shown in Figure 5; the wave field was not strongly modulated by infragravity frequencies in either case, and sediment suspension occurred at incident wave frequencies. Mean sediment concentrations (at z = 0.05 m, $C_{0.05}$) are plotted for all six cases against relative wave height in Figure 6a. For the same relative wave height (H_s/h), $C_{0.05}$ was about a factor of 2 larger for PL cases than for SP cases. The sediment concentration profiles, representing the near-bed sediment load (Figure 7a), further show that near the bed, the profiles appeared straight in log-linear space rather than concave upward, which indicates that for these breaking wave conditions, convective (rather than diffusive) vertical mixing was dominant (Aagaard & Jensen, 2013; Nielsen, 1993).

From the perspective of beach recovery, rates of landward directed, wave-driven sediment transport are important. Net (time-averaged) cross-shore suspended sediment flux at a point in the vertical is calculated as

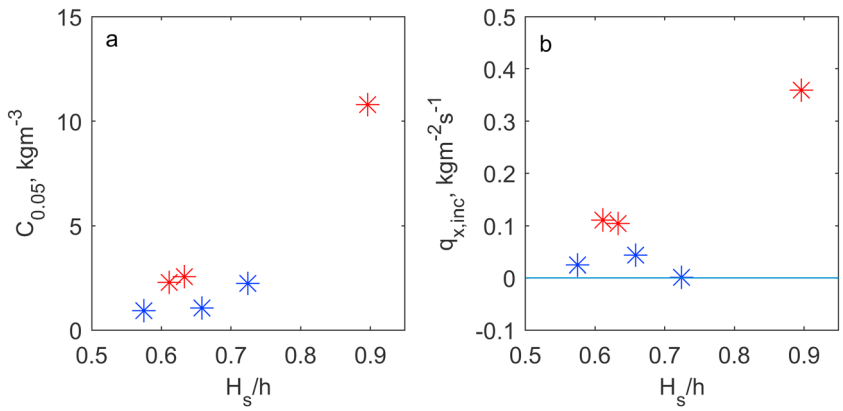

Figure 6. (a) Mean sediment concentration at $z \sim 0.05$ m ($C_{0.05}$) and (b) cross-shore (high-frequency) oscillatory sediment fluxes ($q_{x,\mathrm{inc}}$) at the same elevation, plotted against relative wave height for the six example cases. Red symbols: plunging waves (PL cases); blue symbols: spilling waves (SP cases). Positive $q_{x,\mathrm{inc}}$ is onshore directed.

$$q_x = \frac{1}{T}\int_0^T u(t)c_z(t) \tag{5}$$

where T is the length of an instrument burst time series, $u(t)$ is the instantaneous fluid velocity, and $c_z(t)$ is the instantaneous sediment concentration at an OBS elevation, z. Net suspended sediment transport rates over the vertical can be calculated by summing the fluxes over the vertical. For the six selected records, near-bed sediment fluxes were strikingly different for plunging and spilling cases (Figures 6b and 7b). The net oscillatory (incident wind wave and swell; $f = 0.05$–0.5 Hz) suspended sediment flux ($q_{x,\mathrm{inc}}$) at the lowermost OBS sensor is plotted against H_s/h in Figure 6b. For the same relative wave height, $q_{x,\mathrm{inc}}$ was a factor 3–5 larger for PL cases than for SP cases, and hence, the difference for the two groups of data is more pronounced than the difference in $C_{0.05}$, which shows that sediment flux was more efficient for the plunging wave cases. This is even more evident when considering the vertical profiles of the wave-driven fluxes, that is the near-bed sediment transport (Figure 7b); in the lower 10–15 cm of the water column, transport rates were significantly larger for PL cases and systematically directed onshore over the vertical.

Clearly, a range of other factors (apart from differences in breaker type and processes directly associated with the type of wave breaking, such as turbulence injection) could potentially have affected the sediment load and transport magnitudes. However, sensor elevations were not different for the two groups of data (Figure 7), the mean sediment grain size did not change over the course of the experiment, and it is unlikely that the different transport rates were caused by orbital velocity nonlinearities, since velocity skewness and

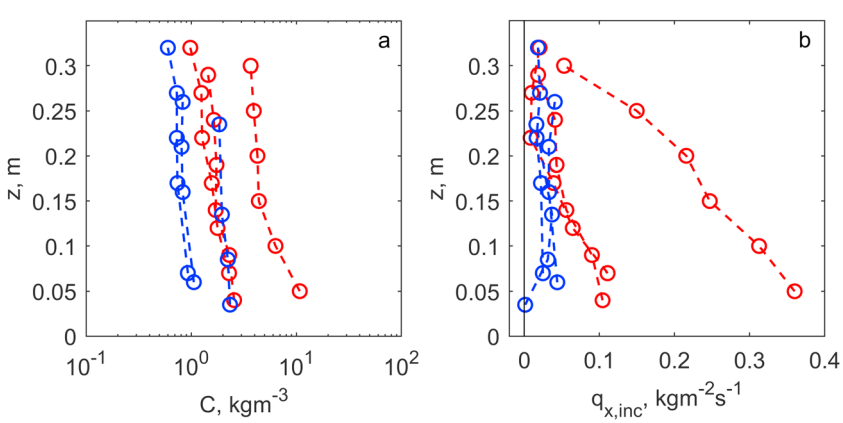

Figure 7. (a) Mean sediment concentrations and (b) cross-shore (high-frequency; $q_{x,inc}$) oscillatory sediment transport rates over the vertical sensor array for the six example cases. Red symbols: PL cases; blue symbols: SP cases.

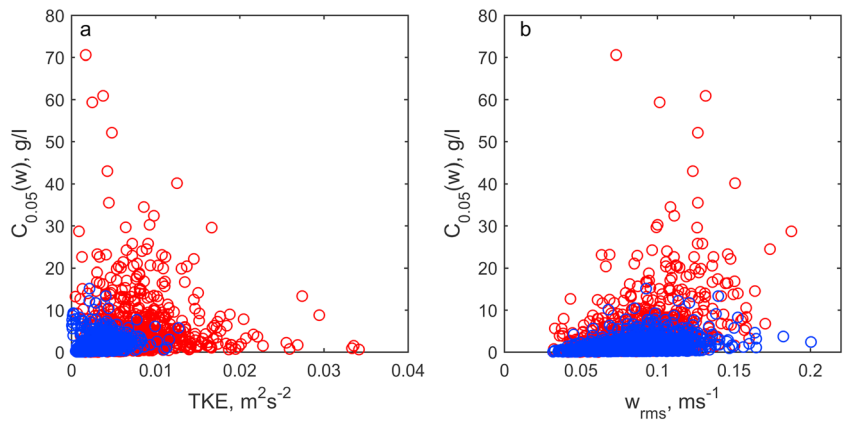

Figure 8. Wave-averaged sediment concentration ($C_{0.05}[w]$) plotted against (a) wave-averaged turbulent kinetic energy and (b) RMS vertical velocity for all waves extracted from the six example time series. Red symbols: PL cases; blue symbols: SP cases. RMS = root-mean-square.

asymmetry were near similar for the PL and the SP cases. This points toward a difference in not only magnitude but also timing of sediment suspension within the wave cycle for the two groups of data, and thus differences in intra-wave variation of sediment concentration, as an explanation for the differences in $q_{x,\mathrm{inc}}$.

4.2. Wave-by-Wave and Intra-wave Analysis of Turbulence and Sediment Suspension

A wave-by-wave analysis was undertaken to examine the effect of turbulence magnitude on sediment suspension and transport under the different types of breaking waves. Individual wind/swell waves were extracted from the time series using a zero-downcrossing technique on the demeaned cross-shore velocity, and the velocity time series were then band-pass filtered at $f = 0.05$–0.5 Hz to avoid contamination from long waves and turbulence. The number of waves extracted for each time series ranged between $N = 291$ and 465. For each wave, the wave-averaged sediment concentration at the lowermost OBS elevation ($C_{0.05}[w]$) was calculated and (wave-averaged) TKE and Reynolds stresses were calculated. A plot of $C_{0.05}(w)$ against TKE is shown in Figure 8a. While both TKE and $C_{0.05}(w)$ were larger for PL compared to SP cases, it is clear that wave-averaged levels of TKE (or $|\tau|$; not shown) demonstrate little or no skill in constraining/explaining near-bed levels of sediment concentration on the timescale of single waves.

Root-mean-square vertical velocity, comprising both oscillatory and turbulent velocity components, was a somewhat better predictor than TKE ($r^2 = 0.11$–0.46 for the six individual cases); however, a universal relationship does not appear to exist. While an increasing trend of $C_{0.05}(w)$ with w_{rms} might be discerned in Figure 8b, there is much scatter and least squares fits are different for the SP and PL cases. Horizontal velocities (not shown) were even less successful in predicting $C_{0.05}(w)$. Thus, it would appear very difficult to predict suspended sediment concentration on a wave-by-wave basis from turbulent (or oscillatory velocity) quantities under irregular breaking waves in the field.

Compared to regular wave (laboratory) conditions, turbulence production and sediment suspension are highly intermittent when measured in the field. Figure 9 shows a short 75-s excerpt of cross-shore and vertical velocities, TKE, and sediment concentration at $z = 0.05$ m ($c_{0.05}[t]$) from PL28. Seven turbulence events ($TKE > 0.05$ m^2/s^2) occurred at $t \sim 348$, 354, 367, 378, 393, 405, and 416 s. Comparing the timings with the cross-shore velocity trace, these turbulence bursts occurred on the front face of the wave, preceding the wave crest and shortly after the velocity zero-upcrossing in all cases. Three of the seven turbulence events were associated with sediment suspension events occurring immediately after the turbulence burst, while in two cases ($t \sim 378$, 406 s), suspension lagged TKE by 1 and 5 s, respectively, and in the latter case, the sediment cloud would appear to have been advected from a location more shoreward. The last two TKE bursts were not clearly associated with a suspension event. Two of these events ($t \sim 348$, 378) are shown in more detail in Figure 10. Maximum TKE-levels preceded the wave crest and were large and short lived. Smaller oscillations occurred prior to and after TKE-peaks, suggesting a coherent vortex structure.

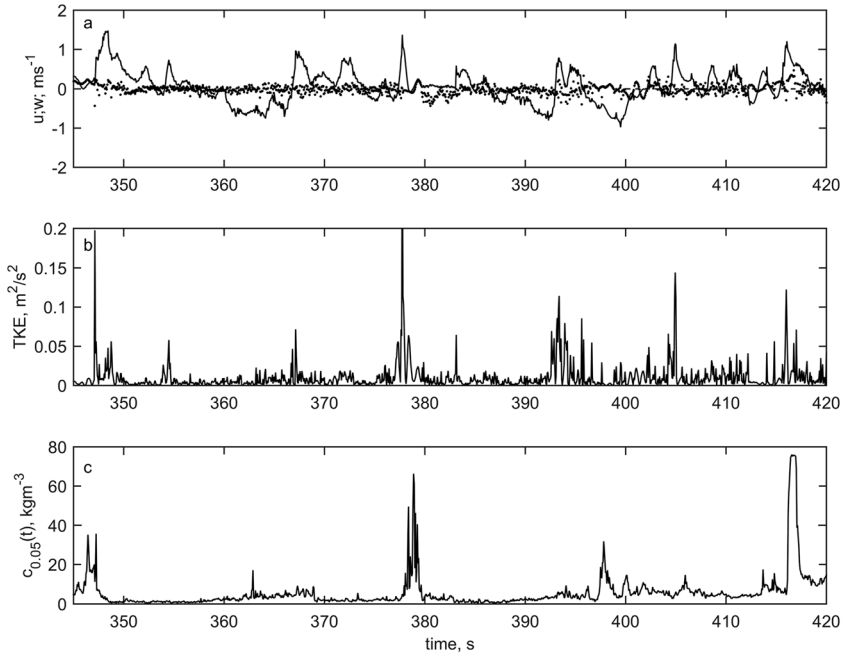

Figure 9. Time series slice from PL28 showing (a) cross-shore (*u*; solid line) and vertical (*w*; dots) velocities, (b) turbulent kinetic energy (TKE), and (c) instantaneous sediment concentration at z = 0.05 m.

Figures 10e and 10f illustrate the boil (at t ~ 379.2) often seen at the back of plunging breakers, which is typically produced by an ascending vortex limb.

A 60-s excerpt from SP42 is representative of spilling wave conditions (Figure 11). Six turbulence events of significantly smaller magnitude than those seen in Figure 9 ($TKE > 0.025$ m^2/s^2) can be identified at

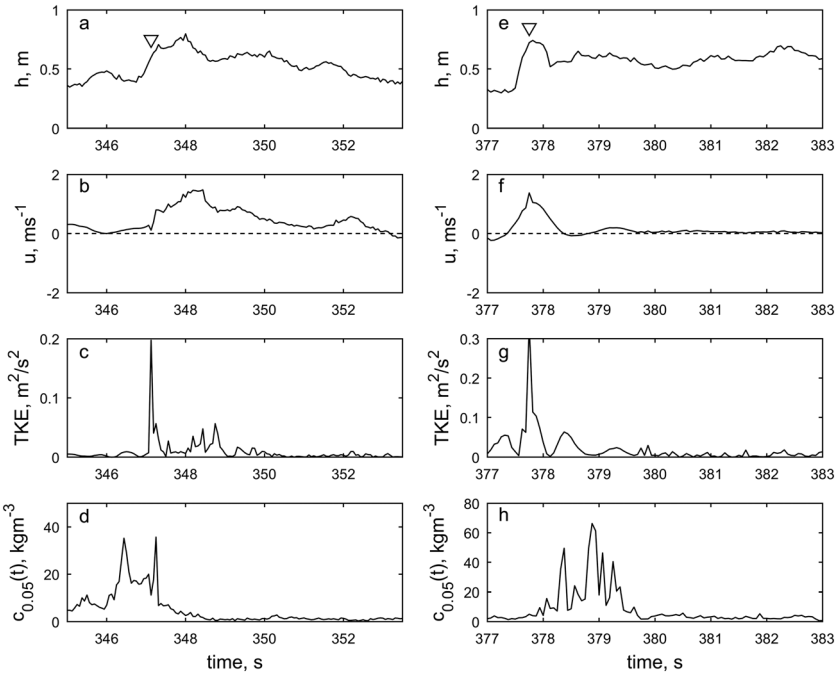

Figure 10. Enlarged detail from Figure 9, showing water depth (a, e), cross-shore current speed (b, f), turbulent kinetic energy (c, g), and near-bed suspended sediment concentration (d, h) under plunging breakers. The triangles in the upper panels indicate the timing of TKE peaks. TKE = turbulent kinetic energy.

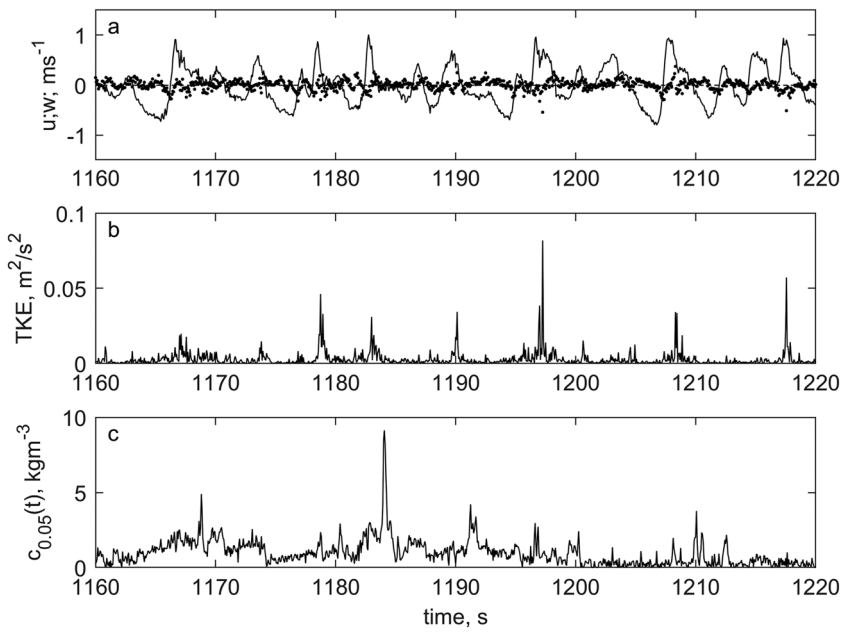

Figure 11. Time series slice from SP42 showing (a) cross-shore (*u*; solid line) and vertical (*w*; dots) velocities, (b) turbulent kinetic energy (TKE), and (c) instantaneous sediment concentration at z = 0.05 m.

t = 1,179; 1,183; 1,190; 1,197; 1,209; and 1,218 s. These events all occurred after the passage of the wave crest, approaching the velocity zero downcrossing. Suspension events (to the extent that such are generated) occurred with a further lag of ~ 1 s after the turbulence burst. Enlarged plots of two of these events (at t ~ 1,197 and 1,209) are shown in Figure 12; TKE clearly peaked some time after the passage of wave crests in these cases.

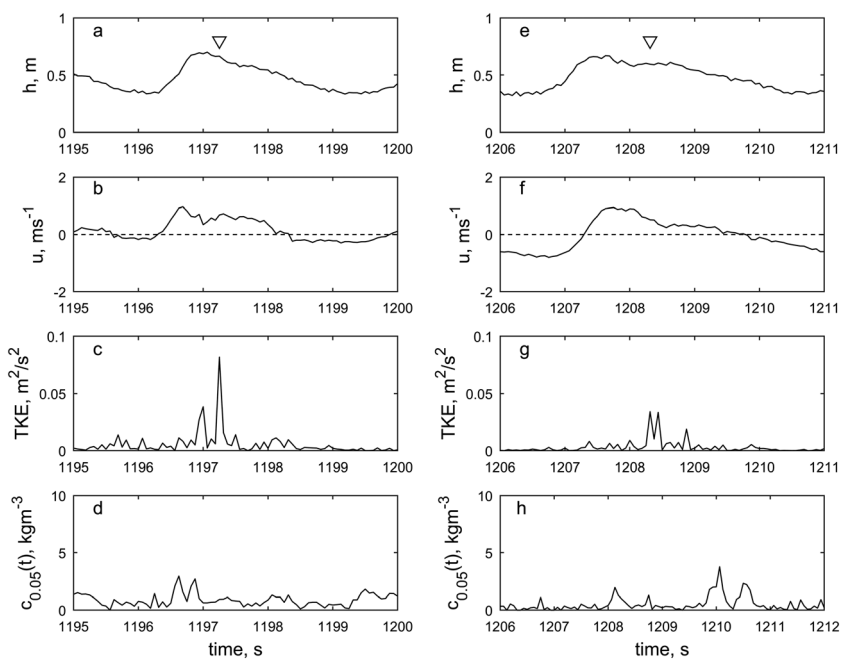

Figure 12. Enlarged detail from Figure 11, showing water depth (a, e), cross-shore current speed (b, f), turbulent kinetic energy (c, g), and near-bed suspended sediment concentration (d, h) under spilling breakers. The triangles in the upper panels indicate the timing of TKE peaks. TKE = turbulent kinetic energy.

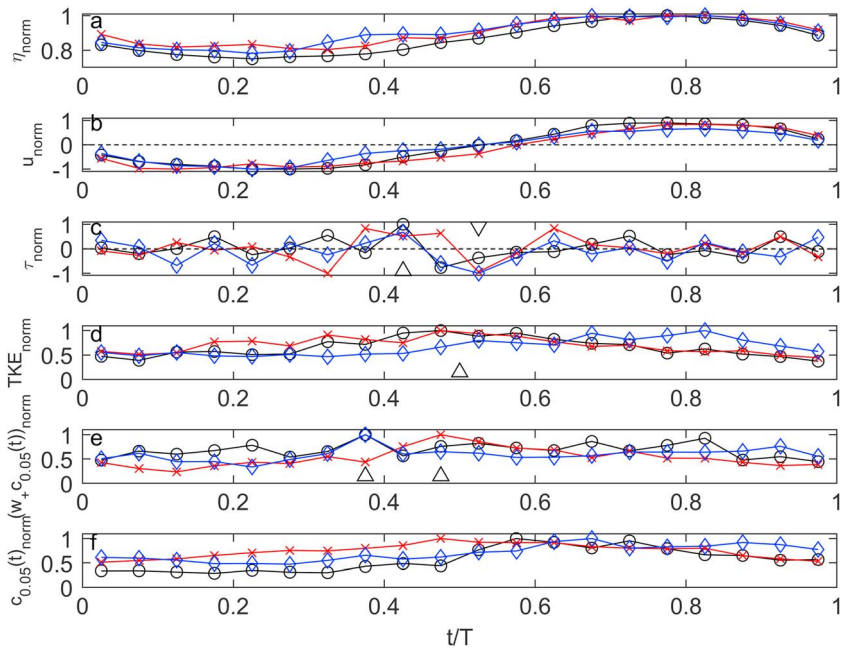

Figure 13. Normalized values of ensemble-averaged (a) surface elevation, η, (b) cross-shore wave orbital velocity, (c) turbulent Reynolds stress (τ), (d) turbulent kinetic energy (TKE), (e) local sediment pickup, and (f) sediment concentration at $z \sim 0.05$ m as a function of relative wave phase (t/T) for the three PL cases. The open triangles point toward maximum values of Reynolds stress, TKE, and sediment pickup. Black circles: PL3; red crosses: PL28; blue diamonds: PL36.

To examine whether these patterns occurred systematically on intra-wave timescale, ensemble-averaged quantities were calculated. For each wave, cross-shore and vertical velocities, sediment concentration, and turbulence measures were extracted and normalized against relative wave phase, t/T, and finally ensemble averaged. Ensemble averaging was carried out using

$$\overline{X}(t) = \frac{1}{N}\sum_{n=0}^{N-1} X(t + nT) \tag{6}$$

where X represents some quantity over time, and N is the number of ensembles. Turbulence and sediment suspension are stochastic and intermittent in an irregular wave field, for example, Nielsen (1993) described the convective suspension over vortex ripples as a *spotted carpet*, and similar patterns were identified for turbulence under breaking waves (Zhou et al., 2014). Hence, we follow Jaffe and Sallenger (1993), Yoon and Cox (2012), and Brinkkemper et al. (2017) and examine only *intense* suspension events, which were observed to contribute a disproportionately large amount of the total sediment suspension in those studies. Intense events are defined by waves during which instantaneous sediment concentration $c_{0.05}(t) > C_{0.05} + 3\sigma_{c_{0.05}(t)}$, where σ is the standard deviation. The number of waves during which intense suspension events occurred ranged between N = 50–88 for the PL cases and N = 30–69 for the SP cases, which corresponded to 16.2% on average (range 6.5–25.4% for the individual records) of the total number of waves in the selected time series. However, these events were responsible for 48.1% (on average; range 40.9–59.9%) of the local sediment pickup, defined as the sediment concentration at the lowermost OBS sensor multiplied by the upward directed (positive) vertical velocity, $w_+(t)c_{0.05}(t)$, and thus corresponding to the upward sediment flux.

Ensemble-averaged surface elevation (η), cross-shore velocity (u), turbulent Reynolds stress ($\tau = \rho|u'|w'$, that is, in this case with the w sign preserved to identify upward/downward motions), TKE, $w_+c_{0.05}(t)$, and $c_{0.05}(t)$ are plotted against relative wave phase (t/T) for the three PL cases (Figure 13). All variables were normalized by their maximum value to facilitate comparison between the examples. Cross-shore velocity reversals (velocity zero-upcrossings) occurred at $t/T \approx 0.55$, and for these intense-event-generating waves, velocity skewness was in fact negative and larger orbital velocities tended to occur in troughs rather than under

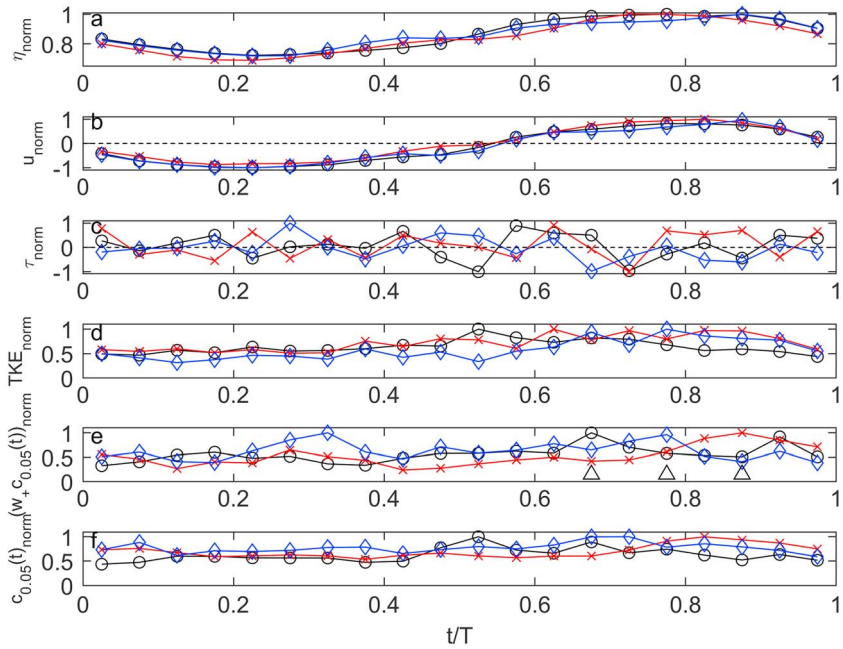

Figure 14. Normalized values of ensemble-averaged (a) surface elevation, η, (b) cross-shore wave orbital velocity, (c) turbulent Reynolds stress (τ), (d) turbulent kinetic energy (TKE), (e) local sediment pickup, and (f) sediment concentration at $z \sim 0.05$ m as a function of relative wave phase (t/T) for the three SP cases. The open triangles point toward maxima of sediment uplift. Black circles: SP16; red crosses: SP42; blue diamonds: SP44.

crests (Figure 13a). Reynolds stress (τ; Figure 13b) exhibited a distinctive pattern with large upward directed stresses on the lower front face of the wave ($t/T \approx 0.42$) immediately prior to velocity reversals. A similar phenomenon was observed under regular plunging breakers by van der Zanden et al. (2018) and ascribed to local turbulence production and a bed-parallel TKE-influx from shoreward locations immediately prior to the arrival of the plunging jet. This is followed by downward directed stresses at velocity reversal ($t/T \approx 0.55$) caused by the plunging jet (van der Zanden et al., 2018), and there is some evidence for turbulent roll-up at $t/T \approx 0.62$–0.72. These latter fluctuations bear the signature of large coherent turbulent vortices associated with plunging breakers. In two cases, TKE increased steadily from the velocity zero-downcrossing and peaked at velocity reversal, followed by a steady decrease (Figure 13d). This is also consistent with observations reported by van der Zanden et al. (2018). For PL36, TKE did exhibit a local maximum at velocity reversal, but a larger maximum occurred under the wave crest. Figure 13e shows local sediment suspension (pickup) from the seabed, $w_+c_{0.05}(t)$. As indicated by the triangles, maximum pickup occurred at $t/T = 0.375$–0.475, which is coincident with the upward directed Reynolds stress slightly preceding the velocity reversal. Thus, maximum turbulence production and sediment uplift both occurred on the front face of the wave. Accordingly, ensemble-averaged sediment concentrations peaked immediately afterward at $t/T = 0.55$–0.65 near or shortly after the velocity zero upcrossing (Figure 13f).

Turbulent signatures were less clear for the SP cases (Figure 14). Cross-shore velocity reversals also occurred at $t/T \sim 0.55$ (Figure 14a). The waves do not resemble sawtooth-shaped surf bores, but we reemphasize that these were not spilling surf bores in the inner surf zone but spilling breakers in the outer surf zone. There is some evidence for upward directed stresses at $t/T \sim 0.57$–0.67 and downward stresses at $t/T \sim 0.67$–0.72 (Figure 14c), again suggestive of vortex structures but occurring significantly later in the wave cycle than for the PL cases. Maximum TKE levels were also achieved later in the wave cycle, in these cases under the wave crest near $t/T \sim 0.75$ (Figure 14d), which would be consistent with a relatively slow downward travel of turbulence (produced on the front face of the wave), as identified for spilling breakers by Nadaoka et al. (1988) and Ting and Kirby (1996). Maximum sediment pickup occurred under the wave crest or shortly thereafter between $t/T \sim 0.67$ and 0.87 (Figure 14e), and

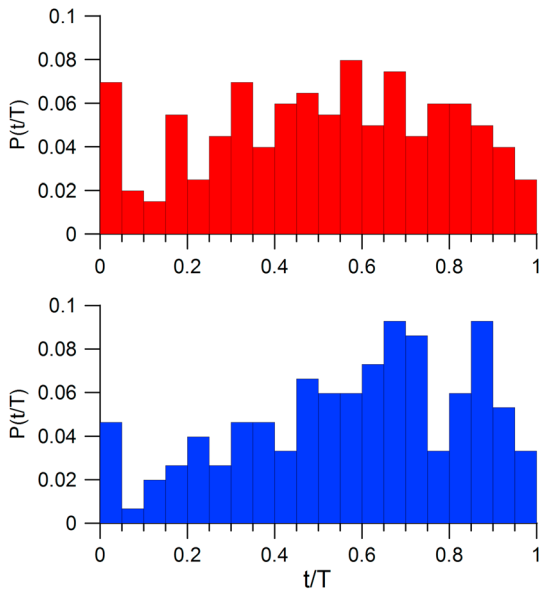

Figure 15. Probability density functions showing relative timing within the wave cycles of maximum TKE for PL (red; n = 201) and SP (blue; n = 153) cases. TKE = turbulent kinetic energy.

accordingly, sediment concentrations at z = 0.035–0.07 m peaked later in the wave cycle than for the PL cases, at t/T = 0.67–0.82 (Figure 14f).

To evaluate the sediment transport potential of the two wave types, the relative near-bed sediment load (i.e., the vertically integrated sediment concentrations over the measurement array; z ~ 0.05–0.3 m) on the onshore (positive velocities) wave phase and the offshore (negative velocities) wave phase was calculated as

$$C_r = \frac{\Sigma C_{u+}}{\Sigma C_{u-}} \tag{7}$$

For the three PL cases, $\overline{C_r}$ = 1.315, while for the three SP cases, $\overline{C_r}$ = 0.937. Hence, the near-bed sediment load was about 32% larger on the wave crest phase compared to the trough phase for the PL cases, while more sediment was available for transport on the trough phase for the SP cases. This difference is probably the main reason for the larger onshore transport rates observed under plunging waves (Figure 7b).

The distribution of TKE-maxima was different for the two populations. The relative timing of maxima within the wave cycle for all intense events (N = 201 and 153 for PL and SP cases, respectively) is shown in histograms in Figure 15. On average, maximum TKE (for individual waves) arrived earlier in the wave cycle ($\overline{t/T} = 0.515$) for PL cases than for SP cases ($\overline{t/T} = 0.571$), and a Wilcoxon rank sum test showed that the two samples and their median ranks were significantly different at α = 0.05 (p = 0.0447).

A universal relationship between turbulence magnitude and sediment concentration did not appear to exist using the wave-by-wave approach (Figure 8). However, the ensemble-averaged plots (Figures 13 and 14) suggest that this may be the case on a wave-phase-averaged basis, at least when considering the intense suspension events that were responsible for approximately 50% of the suspended sediment observed in the time series. Cross-correlation of ensemble-averaged $c_{0.05}(t)$ against TKE is shown in Figure 16 for the six individual example cases. Cross-correlations are all significant (α = 5%; $p > 0.444$) and with small lags between forcing and response ($t/T = \pm 0.2$). As a further test, ensemble-averaged sediment concentrations ($c[t]$ at nominal z = 0.05, 0.15, and 0.25 m) are plotted against ensemble-averaged Froude-scaled TKE ($k[t]$) across all phases of the six example cases in Figure 17. Sediment concentrations were nondimensionalized by assuming a density of 2,650 kg/m^3 and a pore space correction factor of a' = 0.6. Consistent with the wave-by-wave analysis of all waves (Figure 8), the data illustrate that both k and c are larger for plunging than for spilling breakers. But, in contrast to the wave-by-wave analysis, the (ensemble-averaged) intra-wave analysis on intense events suggests that there was a linear relationship between $k(t)$ and $c(t)$, and the PL and SP populations overlap in parameter space. Given the complexities involved in the suspension of sediment under waves, such as the inherent hysteresis in sediment suspension processes and settling, advection by oscillatory and mean currents, and the range in elevations of the individual OBS (estimated at ±1.75 cm; Figure 7), the relatively strong correlation is somewhat surprising. A predictive equation suggests that at z ~ 0.05 m, and above a threshold of k ~ 0.016, $c_{0.05}(t)$ = 0.40 $k(t)$ (r^2 = 0.814) for spilling and plunging breakers in the outer surf zone. At higher elevations, it would be expected that the coefficients of proportionality and the correlations degrade, which is also the case; at z ~ 0.15/0.25 m, $c(t)$ = 0.12 $k(t)$/0.11 $k(t)$ (r^2 = 0.625/0.665). These findings support our hypothesis that magnitude and timing of TKE injection is important in a quantification of suspended sediment transport under breaking waves.

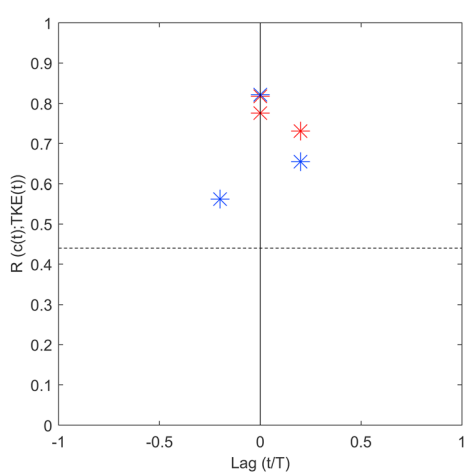

Figure 16. Maximum cross-correlation of ensemble-averaged sediment concentration ($c_{0.05}[t]$) against TKE. Red symbols: PL cases; blue symbols: SP cases. The dashed horizontal line indicates the 5% significance level. TKE = turbulent kinetic energy.

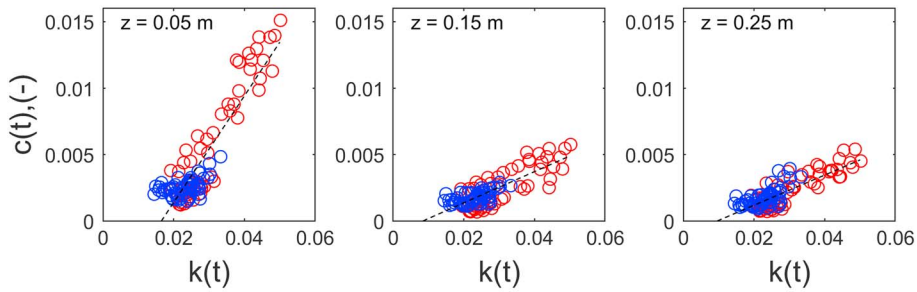

Figure 17. Ensemble-averaged sediment concentrations at (nominally) z = 0.05, 0.15, and 0.25 m, as a function of ensemble-averaged Froude-scaled TKE. Red: PL cases; blue: SP cases. TKE = turbulent kinetic energy.

5. Discussion

The analysis has shown that in the case of irregular waves near the mean breakpoint position, and for similar relative wave heights, mean near-bed suspended sediment concentrations were larger for plunging breakers than for spilling breakers, Figures 6a and 7a. Different breaker types caused an even more significant difference in cross-shore oscillatory (high-frequency) transport rate, which was systematically larger and onshore directed throughout the vertical for PL cases (Figures 6b and 7b). Consistent with earlier limited field observations (Aagaard & Hughes, 2010) and with results from recent large-scale laboratory experiments using irregular waves (Brinkkemper et al., 2017), we observe significant intra-wave variation in suspended sediment concentration under breaking waves. For the intense suspension events, responsible for roughly 50% of the recorded sediment suspension, larger (vertically integrated) sediment loads were attained on the wave crest phase than on the trough phase for plunging breakers ($\overline{C_r}$ = 1.315), while the opposite was the case for spilling breakers ($\overline{C_r}$ = 0.937). Hence, there was a relative difference of 32% in sediment load on the crest phase compared to the trough phase for the two breaker types that resulted in larger onshore sediment transport rates for plunging breakers.

Onshore wave-driven transport under breaking waves in the surf zone is often explained in terms of wave shape asymmetry/acceleration skewness (Austin et al., 2009; Fernandez-Mora et al., 2015), but since there was no large difference in acceleration skewness for SP and PL cases (Table 1), this is a less likely explanation for the very different intra-wave sediment concentrations and very different sediment transport rates observed for the different wave types in this study. Instead, we find that sediment concentration and transport depended on the magnitude and timing of turbulence injection into the water column. TKE levels were larger for PL cases compared to SP cases and peaked earlier within the wave cycle for the PL cases (Figure 15). Both raw time series (Figures 9–12) and the ensemble-averaged intrawave analysis (Figures 13 and 14) indicated that for PL cases, turbulent events were generated on the front face of the wave. This is consistent with injection of large vortices produced by plunging breakers near the breakpoint that were identified in recent large-scale wave flume experiments using regular waves (van der Zanden et al., 2016, 2018). For the SP cases, near-bed turbulence peaked significantly later in the wave cycle, after the passage of the wave crest, which suggests a slower penetration of surface-generated turbulence into the water column. This is consistent with laboratory observations made under spilling waves by Ting and Kirby (1994) and Cox and Kobayashi (2000), and with the expected signature of obliquely descending eddies produced by spilling breakers (Nadaoka et al., 1988). Since suspended sediment concentration is correlated with TKE and with small lag (Figures 16 and 17), the difference in both magnitude and timing of TKE injection was instrumental in driving larger amounts of sand onshore under plunging breakers than under spilling breakers, because larger amounts of sediment were available for transport during the entire crest phase ($\overline{C_r} > 1$).

We infer that conventional models for sediment concentration or sediment pickup that are based on bed shear stress derived from horizontal velocities (e.g., Bailard, 1981; Nielsen et al., 2002) would not be ideal for breaking wave conditions. Sediment pickup and maximum sediment loads occurred well before the arrival of wave crests and were not clearly associated with orbital velocity maxima, particularly for the PL cases (Figures 13e and 13f). Instead, our analysis indicates that suspended sediment load was strongly correlated with turbulence in the water column. For the intense suspension events, Froude-scaled

instantaneous TKE ($k(t)$) appears to be an appropriate predictor of instantaneous sediment concentration for both plunging and spilling breakers (Figure 17); however, the relationship may be better constrained for the PL cases than for the SP cases. A clearer relationship between $k(t)$ and $c(t)$ for our plunging cases might be due to the longer wave periods for the PL cases; T was about a factor 2 longer for PL cases relative to SP cases (Table 1). Longer wave periods would allow sediment to settle out of the water column between wave crests and wave troughs, and by inference, relationships between sediment suspension and its forcing might be less clear for short-period wind- or laboratory-wave conditions.

The results from the present study indicate that breaking-induced turbulence should be incorporated in surf zone sediment transport predictions. This has, in the past, been suggested for transport driven by mean currents (additional turbulence derived from breaking waves causing enhanced sediment concentration; Mocke, 2001; van Rijn, 2007; van der Zanden et al., 2017), but here we show that it is also relevant with respect to oscillatory transport, confirming earlier suggestions by Scott et al. (2009). Modeling of wave-driven (oscillatory) sediment transport under breaking waves would entail, as a first step, scaling the instantaneous (phase averaged) $c(t)$ with TKE(t) or $k(t)$, for example, along the lines illustrated in Figure 17. The next step would then be to relate TKE(t) (or $k[t]$) to, for example, (ensemble averaged) orbital velocity, $u(t)$; this is, however, beyond the scope of the present paper.

The scaling of c on k (Figure 17) clearly depends on a robust estimation of k in our data. Instantaneous (phase-averaged) values of Froude-scaled TKE ranged from $k(t) = 0.015$ to 0.05 with time-averaged $\overline{k} = 0.017$–0.024 for SP cases and 0.023–0.043 for PL cases. This is comparable to, but perhaps slightly smaller, than levels of $\overline{k}$ observed under recent controlled laboratory conditions. In the midwater column, van der Zanden et al. (2016) observed $\overline{k} = 0.043$ for regular plunging waves at the bar crest, while Brinkkemper et al. (2016) reported $\overline{k} = 0.02$–0.06 for irregular laboratory waves. Different techniques were used to estimate turbulence levels in this study, which might have affected calculations of $\overline{k}$ (and $k[t]$). Nevertheless, the clear relationship between $k(t)$ and $c(t)$ suggests that our method to extract turbulence from velocity records is not grossly in error and, if k is indeed underestimated, this would only change the constant of proportionality in Figure 17.

The differences in breaker type and hence the difference in timing of turbulence injection, intra-wave variations in sediment load, and wave-driven sediment transport is probably related to more general environmental boundary conditions. For temporally non-homogeneous rates of turbulence injection and sediment uplift, it is likely that sediment grain size and wave period do affect the relative sediment loads on wave crest and trough phases, and hence $q_{x,\mathrm{inc}}$, by allowing sediment to settle between bursts of suspension. The Gourlay-parameter ($\Omega = H_s/w_sT$, where w_s is sediment settling velocity) is a measure of sediment uplift versus settling tendencies, and it was originally derived to predict offshore versus onshore sediment transport (Dean, 1973; Gourlay, 1968). For the data used here, Ω was a factor of 2–3 smaller for PL cases compared to SP cases (Table 1), indicating a theoretically stronger tendency toward onshore transport of sediment. Future work will investigate the effects of wave period and grain size on sediment suspension and transport under breaking waves in the field.

6. Conclusions

The work reported here has shown that for irregular wave conditions in the outer surf zone, suspended sediment concentrations, and especially onshore-directed wave-driven suspended sediment transport rates are significantly larger for plunging compared to spilling breakers. This is at least partly due to (i) higher levels of TKE and larger sediment loads under plunging compared to spilling breakers, and (ii) earlier injection of turbulence into the water column under plunging breakers. In PL cases, maximum TKE-injection occurred on the front face of the wave, while the appearance of turbulence at the seabed occurred later and over a larger part of the wave cycle under spilling breakers. The result was a larger difference in cumulated sediment load under the wave crest phase compared to the wave trough phase for plunging breakers. Although we cannot identify the turbulence source (due to a lack of a vertical turbulence measurement array), we infer that TKE was mainly produced by the breaking waves, and this is consistent with both the timing and temporal behavior of the measured Reynolds stress, as observed by van der Zanden et al. (2018) and Cox and Kobayashi (2000) for plunging and spilling breakers, respectively. While it would appear highly challenging to parameterize sediment load for individual waves, analysis of ensemble-averaged intense

suspension events suggested that above a threshold of $k \approx 0.015$, near-bed suspended sediment concentration under breaking waves (in the outer surf zone) scales with k; $c_{0.05}(t) \approx 0.4\ k(t)$. At higher elevations above the bed, concentration still scales with k but with a smaller coefficient of proportionality, as expected. Hence, the results may partially explain the long-held view that relatively long-period swell waves, typically associated with plunging breakers, are often associated with net onshore transport and beach accretion.

Acknowledgments
The present work was supported by the Danish Natural Sciences Research Council, grants 272-05-0415 and 4181-00045. The depth, velocity, and sediment concentration data are available from the Dryad Digital Repository (https://doi.org/10.5061/dryad.mv711kb). We wish to thank Aart Kroon, Brian Greenwood, Stine Gro Jensen, Tom Baldock, and Dave Mitchell for their assistance and good cheer during the field campaign. Hotel Senator provided shelter and computer space in the field and was kindly put at our disposal by the Department of Forestry and Nature at Varde. We thank the Associate Editor and three anonymous reviewers for their helpful comments on an earlier version of the manuscript.

References

Aagaard, T., & Hughes, M. G. (2010). Breaker turbulence and sediment suspension in the surf zone. *Marine Geology*, *271*(3-4), 250–259. https://doi.org/10.1016/j.margeo.2010.02.019

Aagaard, T., & Jensen, S. G. (2013). Sediment concentration and vertical mixing under breaking waves. *Marine Geology*, *336*, 146–159. https://doi.org/10.1016/j.margeo.2012.11.015

Austin, M., Masselink, G., O'Hare, T., & Russell, P. (2009). Onshore sediment transport on a sandy beach under varied wave conditions: Flow velocity skewness, wave asymmetry or bed ventilation? *Marine Geology*, *259*(1-4), 86–101. https://doi.org/10.1016/j.margeo.2009.01.001

Bailard, J. A. (1981). An energetics total load sediment transport model for a plane sloping beach. *Journal of Geophysical Research*, *86*(C11), 10,938–10,954. https://doi.org/10.1029/JC086iC11p10938

Battjes, J. A. (1974). *Surf similarity*, *Proceedings 14th Coastal Eng. Conf.* (pp. 466–479). New York: American. Society of. Civil Engineers.

Brinkkemper, J. A., de Bakker, A. T. M., & Ruessink, B. G. (2017). Intrawave sand suspension in the shoaling and surf zone of a field-scale laboratory beach. *Journal of Geophysical Research: Earth Surface*, *122*, 356–370. https://doi.org/10.1002/2016JF004061

Brinkkemper, J. A., Lanckriet, T., Grasso, F., Puleo, J. A., & Ruessink, B. G. (2016). Observations of turbulence within the surf and swash zones of a field-scale sandy laboratory beach. *Coastal Engineering*, *113*, 62–72. https://doi.org/10.1016/j.coastaleng.2015.07.006

Chassagneux, F. X., & Hurther, D. (2014). Wave bottom boundary layer processes below irregular surfzone breaking waves with light-weight sheet flow particle transport. *Journal of Geophysical Research: Oceans*, *119*, 1668–1690. https://doi.org/10.1002/2013JC009338

Cox, D. T., & Kobayashi, N. (2000). Identification of intense, intermittent coherent motions under shoaling and breaking waves. *Journal of Geophysical Research*, *105*(C6), 14,223–14,236. https://doi.org/10.1029/2000JC900048

Dean, R. G. (1973). Heuristic models of sand transport in the surf zone. 1st Australian Conference on Coastal Engineering (pp. 208–214).

Dingler, J. R., & Inman, D. L. (1976). *Wave-formed ripples in nearshore sands*. *Proc. 15th International Conference on Coastal Engineering* (pp. 2109–2126). New York: American Society of Civil Engineers.

Elgar, S., Raubenheimer, B., & Guza, R. T. (2005). Quality control of acoustic Doppler velocimeter data in the surfzone. *Measurement Science and Technology*, *16*(10), 1889–1893. https://doi.org/10.1088/0957-0233/16/10/002

Emery, W. J., & Thompson, R. E. (2001). *Data analysis methods in physical oceanography* (2nd ed., p. 638). Amsterdam: Elsevier.

Fernandez-Mora, A., Calvete, D., Falques, A., & de Swart, H. E. (2015). Onshore sandbar migration in the surf zone: New insights into the wave-induced sediment transport mechanisms. *Geophysical Research Letters*, *42*, 2869–2877. https://doi.org/10.1002/2014GL063004

Foster, D. L., Beach, R. A., & Holman, R. A. (2006). Turbulence observations of the nearshore wave bottom boundary layer. *Journal of Geophysical Research*, *111*, C04011. https://doi.org/10.1029/2004JC002838

Glenn, S. M., & Grant, W. D. (1987). A suspended sediment stratification correction for combined wave and current flows. *Journal of Geophysical Research*, *92*(C8), 8244–8264. https://doi.org/10.1029/JC092iC08p08244

Gourlay, M. R. (1968). Beach and dune erosion tests. Delft Hydraulics Laboratory, Report no. M935/M936.

Grasso, F., & Ruessink, B. G. (2012). Turbulent viscosity in natural surf zones. *Geophysical Research Letters*, *39*, L23603. https://doi.org/10.1029/2012GL054135

Hay, A. E., & Mudge, T. (2005). Principal bed states during SandyDuck97: Occurrence, spectral anisotropy, and the bed state storm cycle. *Journal of Geophysical Research*, *110*, C03013. https://doi.org/10.1029/2004JC002451

Henderson, S. M., Allen, J. S., & Newberger, P. A. (2004). Nearshore sandbar migration predicted by an eddy-diffusive boundary layer model. *Journal of Geophysical Research*, *109*, C06024. https://doi.org/10.1029/2003JC002137

Jaffe, B., & Sallenger, A. H. (1993). *The contribution of suspension events to sediment transport in the surf zone*. *Proceedings 23rd Coastal Engineering Conference, Venice* (pp. 2680–2693). New York: American Society of Civil Engineers.

Jensen, S. G., Aagaard, T., Baldock, T., Kroon, A., & Hughes, M. G. (2009). Berm formation on a gently sloping accretionary beach. *Earth Surface Processes and Landforms*, *34*(11), 1533–1546. https://doi.org/10.1002/esp.1845

LeClaire, P. D., & Ting, F. C. K. (2017). Measurements of suspended sediment transport and turbulent coherent structures induced by breaking waves using two-phase volumetric three-component velocimetry. *Coastal Engineering*, *121*, 56–76. https://doi.org/10.1016/j.coastaleng.2016.11.008

Marino-Tapia, I. J., O'Hare, T. J., Russell, P. E., Davidson, M. A., & Huntley, D. A. (2007). Cross-shore sediment transport on natural beaches and its relation to sandbar migration patterns: 2. Application of the field transport parameterization. *Journal of Geophysical Research*, *112*, CO3002. https://doi.org/10.1029/2005JC002894

Mocke, G. P. (2001). Structure and modeling of surf zone turbulence due to wave breaking. *Journal of Geophysical Research*, *106*(C8), 17,039–17,057. https://doi.org/10.1029/2000JC900163

Nadaoka, K., Hino, M., & Koyano, Y. (1989). Structure of the turbulent flow field under breaking waves in the surf zone. *Journal of Fluid Mechanics*, *204*(1), 359–387. https://doi.org/10.1017/S0022112089001783

Nadaoka, K., Ueno, S., & Igarashi, T. (1988). *Sediment suspension due to large scale eddies in the surf zone*. *Proceedings 21st Coastal Engineering Conference* (pp. 1646–1660). New York: American Society of Civil Engineers.

Nielsen, P. (1992). *Coastal bottom boundary layers and sediment transport* (324 pp.). Singapore: World Scientific. https://doi.org/10.1142/1269

Nielsen, P. (1993). *Combined convection-diffusion modelling of sediment entrainment*. *Proceedings 23rd Coastal Engineering Conference* (pp. 3202–3215). New York: American Society of Civil Engineers.

Nielsen, P., van der Wal, K., & Gillan, L. (2002). Vertical fluxes of sediment in oscillatory sheet flow. *Coastal Engineering*, *45*(1), 61–68. https://doi.org/10.1016/S0378-3839(01)00043-6

Ruessink, B. G. (2010). Observations of turbulence within a natural surf zone. *Journal of Physical Oceanography*, *40*(12), 2696–2712. https://doi.org/10.1175/2010JPO4466.1

Ruessink, B. G., Kuriyama, Y., Reniers, A. J. H. M., Roelvink, J. A., & Walstra, D. J. R. (2007). Modeling cross-shore sandbar behaviour on the timescale of weeks. *Journal of Geophysical Research*, *112*, F03010. https://doi.org/10.1029/2006JF000730

Scott, N. V., Hsu, T.-J., & Cox, D. (2009). Steep wave, turbulence and sediment concentration statistics beneath a breaking wave field and their implications for sediment transport. *Continental Shelf Research*, *29*(20), 2303–2317. https://doi.org/10.1016/j.csr.2009.09.008

Shaw, W. E., & Trowbridge, J. H. (2001). The direct estimation of near-bottom turbulent fluxes in the presence of energetic wave motions. *Journal of Atmospheric and Oceanic Technology*, *18*(9), 1540–1557. https://doi.org/10.1175/1520-0426(2001)018<1540:TDEONB>2.0.CO;2

Shin, S., & Cox, D. (2006). Laboratory observations of inner surf and swash-zone hydrodynamics on a steep slope. *Continental Shelf Research*, *26*(5), 561–573. https://doi.org/10.1016/j.csr.2005.10.005

Sumer, B. M., Guner, H. A. A., Hansen, N. M., Fuhrman, D. R., & Fredsøe, J. (2013). Laboratory observations of flow and sediment transport induced by plunging regular waves. *Journal of Geophysical Research: Oceans*, *118*, 6161–6182. https://doi.org/10.1002/2013JC009324

Ting, F. C. K. (2013). Laboratory measurements of large-scale near-bed turbulent flow structures under plunging regular waves. *Coastal Engineering*, *77*, 120–139. https://doi.org/10.1016/j.coastaleng.2013.02.014

Ting, F. C. K., & Kirby, J. T. (1994). Observation of undertow and turbulence in a laboratory surf zone. *Coastal Engineering*, *24*(1-2), 51–80. https://doi.org/10.1016/0378-3839(94)90026-4

Ting, F. C. K., & Kirby, J. T. (1996). Dynamics of surf zone turbulence in a spilling breaker. *Coastal Engineering*, *27*(3-4), 131–160. https://doi.org/10.1016/0378-3839(95)00037-2

van der A, D. A., van der Zanden, J., O'Donoghue, T., Hurther, D., Caceres, I., McLelland, S. J., & Ribberink, J. S. (2017). Large-scale laboratory study of breaking wave hydrodynamics over a fixed bar. *Journal of Geophysical Research: Oceans*, *122*, 3287–3310. https://doi.org/10.1002/2016JC012072

van der Werf, J. J., Doucette, J. S., O'Donoghue, T., & Ribberink, J. S. (2007). Detailed measurements of velocities and suspended sand concentrations over full-scale ripples in regular oscillatory flow. *Journal of Geophysical Research*, *112*, F02012. https://doi.org/10.1029/2006JF000614

van der Zanden, J., Fernandez-Mora, A., van der A, D., Hurther, D., Caceres, I., O'Donoghue, T., & Ribberink, J. (2017). Inclusion of wave breaking turbulence in reference concentration models. Proceedings Coastal Dynamics 2017, Helsingør, Denmark, paper 188 (pp. 629–641).

van der Zanden, J., van der A, D., Caceres, I., Hurther, D., McLelland, S. J., Ribberink, J. S., & O'Donoghue, T. (2018). Near-bed turbulent kinetic energy budget under a large-scale plunging breaking wave over a fixed bar. *Journal of Geophysical Research: Oceans*, *123*, 1429–1456. https://doi.org/10.1002/2017JC013411

van der Zanden, J., van der, A., Hurther, D., Caceres, I., O'Donoghue, T., & Ribberink, J. S. (2016). Near-bed hydrodynamics and turbulence below a large-scale plunging breaking wave over a mobile barred bed profile. *Journal of Geophysical Research: Oceans*, *121*, 6482–6506. https://doi.org/10.1002/2016JC011909

van Rijn, L. C. (2007). Unified view of sediment transport by currents and waves. II: Suspended transport. *Journal of Hydraulic Engineering*, *133*(6), 668–689. https://doi.org/10.1061/(ASCE)0733-9429(2007)133:6(668)

Yoon, H.-D., & Cox, D. T. (2012). Cross-shore variation of intermittent sediment suspension and turbulence induced by depth-limited wave breaking. *Continental Shelf Research*, *47*, 93–106. https://doi.org/10.1016/j.csr.2012.07.001

Zhou, Z., Sangermano, J., Hsu, T.-J., & Ting, F. C. K. (2014). A numerical investigation of wave-breaking-induced turbulent coherent structure under a solitary wave. *Journal of Geophysical Research: Oceans*, *119*, 6952–6973. https://doi.org/10.1002/2014JC009854